PAPER

An asymmetric supercapacitor based on controllable WO₃ nanorod bundle and alfalfa-derived porous carbon†

Kanjun Sun,[*a] Fengting Hua,[b] Shuzhen Cui,[b] Yanrong Zhu,[a] Hui Peng [ID][b] and Guofu Ma [ID] [*b]

A novel asymmetric supercapacitor (ASC) is assembled on the basis of an inerratic hexagonal-like WO₃ nanorod bundle as a negative electrode and graphene-like alfalfa-derived porous activated carbon (APAC) as the positive electrode in 1 M H₂SO₄ aqueous electrolyte. The WO₃ nanostructures prepared at pH of 1.6, 1.8, 2.0, 2.5 and 3.0 display hexagonal disc-like, nanorod bundle, inerratic hexagonal-like, sphere-like, and needle-shaped nanorod morphology. WO₃-2.0, which was prepared at a pH of 2.0, exhibits high specific capacitance (415.3 F g⁻¹ at 0.5 A g⁻¹). APAC-2, which had the mass ratios of dried alfalfa and ZnCl₂ as 1 : 2, showed a 3D porous structure, large surface area (1576.3 m² g⁻¹), high specific capacitance (262.1 F g⁻¹ at 0.5 A g⁻¹), good cycling stability with 96% of initial specific capacitance after 5000 consecutive cycles. The ASC assembled with WO₃-2.0 and APAC-2 exhibits high energy density (27.3 W h kg⁻¹ at a power density of 403.1 W kg⁻¹), as well as good electrochemical stability (82.6% capacitance retention after 5000 cycles). Such outstanding electrochemical behavior implies that the electrode materials are promising for practical energy-storage systems.

1. Introduction

Due to the rapid development of the global economy, there is an urgent need to develop clean and efficient renewable energy.[1] Certainly, sustainable energy storage devices, such as batteries and supercapacitors, continue to maintain the guiding energy model for world energy use, as in the past few decades.[2–5] Unlike batteries, supercapacitors have some advantages such as faster charging, long indefinite lifespan, wide operating temperature range, and nontoxicity in nature.[6–9] In recent years, their application in military equipment and urban rail transit has attracted great attention. Supercapacitors are typically composed of two electrodes (positive and negative), a current collector, an electrolyte (aqueous or organic) and a separator that permits the transfer of ions while keeping the electrodes insulated from each other. Based on the mechanism of charge storage, supercapacitors can be divided into two types: electrochemical double-layer capacitors (EDLCs) and faradaic supercapacitors (FSs). In EDLCs, the charges are stored because of the surface adsorption of the ions from the electrolyte as a result of electrostatic attraction, thus forming two charged layers (double layer). Faradaic pseudocapacitors store charges through fast and reversible oxidation/reduction reactions occurring at the electrode/electrolyte interfaces, as well as in the bulk near the surface of the electrode. EDLCs have outstanding cycle stability, making them widely used in commercial supercapacitors. However, pseudocapacitors show higher capacitance as compared to EDLCs due to the additional charges transferred within the defined potential. However, due to the degradation of the active material in the Faraday reaction, its cycle stability is inferior.[10,11] Furthermore, the electrode material is the most important aspect of the composition for supercapacitors.

Currently, pseudocapacitors based on transition metal (W, Zn, Mn, Fe, Co, Mo, *etc.*) oxides possess high specific capacitance and power density due to their fast and reversible electron transfer redox reactions; for example, MoSe₂,[12] Co(OH)₂,[13] ZnO[14] and so on. Furthermore, WO₃ electrode material has attracted considerable interest in the development of supercapacitors. Lu *et al.* synthesized WO₃₋ₓ@Au@MnO₂ core–shell nanowires (NWs) on a flexible carbon fabric, which showed outstanding electrochemical performance in supercapacitors.[15] Jo *et al.* synthesized ordered mesoporous WO₃₋ₓ/carbon nanocomposites *via* a simple one-pot method using polystyrene-*block*-poly (ethylene oxide) (PS-b-PEO) as a structure-directing agent. It showed high capacitance and enhanced rate performance. In addition, carbon materials prepared from

aCollege of Chemistry and Environmental Science, Lanzhou City University, Lanzhou 730070, China. E-mail: Sunkj@lzcu.edu.cn; Fax: +86 931 7975121; Tel: +86 931 7975121

bKey Laboratory of Eco-Environment-Related Polymer Materials of Ministry of Education, Key Laboratory of Polymer Materials of Gansu Province, College of Chemistry and Chemical Engineering, Northwest Normal University, Lanzhou 730070, China. E-mail: magf@nwnu.edu.cn

† Electronic supplementary information (ESI) available. See DOI: 10.1039/d1ra04788d

agricultural by-product biomass wastes are widely used as electrode materials for supercapacitors due to their large specific surface area, good electrical conductivity and low cost.[16] Importantly, it is cheap, abundant, environmentally safe, commercially available and a sustainable biological resource. For instance, sorghum stalk,[17] prawn shells,[18] coconut shells,[19] and fungus.[20] Gao *et al.* fabricated nitrogen-doped activated carbons by simultaneous carbonization and KOH activation of chitosan biomass regenerated from prawn shells at high temperature. It exhibited high specific capacitance of 695 F g^{-1} in 1 M H_2SO_4 and 357 F g^{-1} in 6 M KOH at a current density of 50 mA g^{-1}.[18] Sun *et al.* synthesized porous graphene-like nanosheets (PGNSs) with a large surface area *via* an easy and cost-effective simultaneous activation–graphitization route from renewable biomass waste coconut shell. PGNSs exhibit outstanding electrochemical performance.[19]

Despite the advantages of high power density and much higher cycle life in pseudocapacitors and EDLCs, their intrinsically low energy density has limited their widespread commercial applications.[21–23] Considering a win–win situation where the fundamental principles behind batteries and supercapacitors work together to reach the common goal of higher energy density and power density. Asymmetric supercapacitors (ASCs) have become prospective energy storage devices. These consist of two different electrodes, *i.e.*, a battery-type faradaic electrode as an energy source and a capacitor-type electrode as a power source, thereby obtaining a supercapacitor with high energy density. The ASC can store a greater amount of energy than the symmetric supercapacitor; most of the existing examples of this category, such as in the case of Zhao *et al.* who assembled and installed a novel asymmetric supercapacitor multicomponent $MnCo_2O_4@Ni(OH)_2$ belt-based core–shell nanoflowers as the anode and an activated-carbon film as the cathode, which demonstrated excellent electrochemical performance.[24] Pan *et al.* reported a facile method to construct nanoporous Ni architecture on the surfaces of flexible carbon cloth (Ni@CC) by electrodeposition of ultrathin MnO_x nanosheets on the 3D Ni@CC nanoporous current collectors (MnO_x@Ni@CC). They employed 3D MnO_x@Ni@CC as a positive electrode and a chemically converted graphene (CCG) as a negative electrode and assembled asymmetric supercapacitor (ASC) to achieve a superior energy density of 1.16 mW h cm^{-3} at a current density of 1 mA cm^{-2}.[25] Among the many active materials, tungsten oxide is one kind of transition metal oxide, which has advantages of low cost, very low toxicity and natural abundance. In particular, tungsten oxides have abundant resources in nature and possess multiple valence states, which will enable various reversible redox reactions, resulting in high electrochemical energy storage behavior for lithium-ion batteries and supercapacitors.[26,27]

In this study, we synthesized nanostructured electrode materials (WO_3-X) with different morphologies at different pH by using a simple hydrothermal method. WO_3-2.0 has higher capacitance due to the low diffusion paths and easy intercalation/de-intercalation of electrolyte ions, thereby improving the electrochemically active surface area. In addition, we designed and synthesized alfalfa-based porous

activated carbon (APACs) with a high S_{BET} value *via* an effective simultaneous activation–graphitization (SAG) route. In the synthesis, the graphitic catalyst precursor ($FeCl_3$) and activating agent ($ZnCl_2$) were simultaneously introduced into the skeleton of alfalfa through the coordination of the metal precursor with functional groups in alfalfa, thus making the simultaneous realization of activation and graphitization of the carbon source under heat treatment. Notably, the iron catalyst in the framework of the alfalfa can generate a carburized phase, which plays a key role in the formation of a graphene-like structure during the pyrolytic process.[28] After that, we assembled an aqueous electrolyte ASC with an excellent electrochemical performance by using hexagon nanostructures pseudocapacitive materials WO_3-2.0 as the negative electrode and graphene-like nanosheets APAC-2 based on alfalfa as the positive electrode in aqueous H_2SO_4 electrolyte.

2. Experimental

2.1. Materials

Solutions of sodium chloride (NaCl, Tianjing Chemical Co., China) and sodium tungstate dihydrate ($Na_2WO_4 \cdot 2H_2O$, Aladdin Ltd. Shanghai China), alfalfa (collected from the local environment, Lanzhou Gansu province, China), zinc chloride ($ZnCl_2$, Aladdin Ltd., Shanghai Chemical Works, China), ferric chloride ($FeCl_3$, Shanghai Chemical Works, China) were prepared using deionized water. All the reagents used in experiments were of analytical grade and used without further purification.

2.2. Synthesis of WO_3 microstructures at different pH values

In a typical process, 2.0 g of sodium tungstate dihydrate and 0.5 g sodium chloride were dissolved in 60 mL deionized water, and 3 M HCl aqueous solution was used to adjust different pH values (1.6, 1.8, 2.0, 2.5 and 3.0) under violent stirring. After stirring for 2 h, the solution was transferred into a 100 mL Teflon-lined stainless-steel autoclave and heated at 180 °C for 24 h. After being cooled to room temperature naturally, the resulting precipitates of WO_3 were collected by filtration, washed with distilled water and absolute ethanol several times, and dried in a vacuum at 60 °C. The obtained samples with different pH values were designated as WO_3-X (WO_3-1.6, WO_3-1.8, WO_3-2.0, WO_3-2.5 and WO_3-3.0).

2.3. Preparation of alfalfa-based porous activated carbon (APAC)

APAC materials with a large surface area were synthesized *via* an effective simultaneous activation–graphitization route, using $ZnCl_2$, $FeCl_3$ and alfalfa as the activating agent, graphitic catalyst precursor and carbon source, respectively. The carbonization, graphitization and activation processes were simultaneously carried out in a tubular furnace. In a typical synthesis, 1.0 g of the dried alfalfa powder was mixed with $ZnCl_2$ (in variable mass ratios of 1 : 0, 1 : 1, 1 : 2 and 1 : 3) and 1.0 g of $FeCl_3$ was ground to form an evenly dispersed mixture. Then, the mixture was placed in a porcelain boat and carbonized in

a tubular furnace at 800 °C for 2 hours (heating rate of 5 °C min^{-1}) in a nitrogen atmosphere. After being cooled to room temperature naturally, the products were thoroughly washed with 2 M HCl to remove iron species, inorganic salts and other impurities thoroughly then dried at 60 °C for 24 h. The obtained samples with different contents of $ZnCl_2$ were designated as APAC-0, APAC-1, APAC-2 and APAC-3.

Structural characterization and electrochemical performance testing are presented in the ESI.†

3. Results and discussion

3.1. Characterizations of WO$_3$-2.0 nanorod bundle negative electrode materials

The morphologies of the synthesized WO$_3$-X were investigated using SEM. From Fig. 1, it can be clearly observed that the size and shape of WO$_3$-X architectures generally depend on the different values of pH employed, as pH is the most important process parameter in the precipitation process, and it directly affects the formation and growth of crystal particles. Controlling the pH value can effectively control the morphology of the particles. As the pH value of the precipitation increases, the primary particles are gradually refined, the sphericity of the particles becomes better, and the tap density of the precursor samples gradually increases, so the obtained morphologies are different.[29] Fig. 1a displays hexagonal disc-like material with protruding surfaces that was prepared using 3 M HCl to adjust the pH value to 1.6 for WO$_3$-1.6. WO$_3$-1.8 products are formed at a reaction pH of 1.8 (Fig. 1b), which exhibits truss shape and bundled feature of nanorod bundles morphology and makes up of many highly ordered nanorods with a length of 200–500 nm. As shown in Fig. 1c and d, it can be clearly seen that the WO$_3$-2.0 sample synthesized at pH 2.0 is an irregular hexagon with a diameter of 5–15 μm composed of many highly ordered nanorod bundles. The unique architecture of the WO$_3$-2.0 irregular hexagon was further confirmed using transmission electron microscopy (TEM) and the results are shown in Fig. S1.† The WO$_3$-2.5 samples synthesized at a pH of 2.5 (Fig. 1d) have sphere-like morphology and approximately 1 mm diameter with intertwined sheet-like subunits. When the pH value was 3.0 (Fig. 1f), WO$_3$-3.0 was composed of some well-aligned thinner one-dimensional (1D) needle-shaped
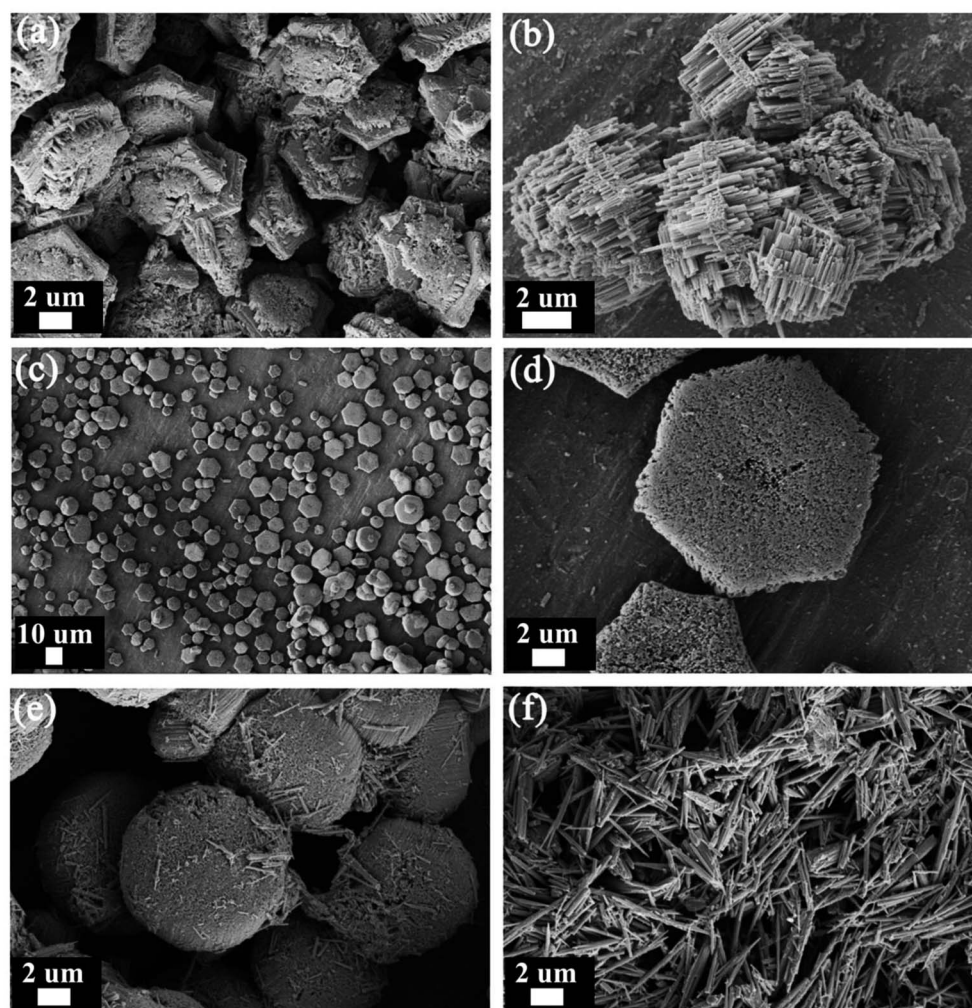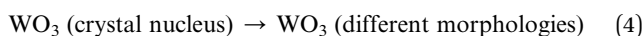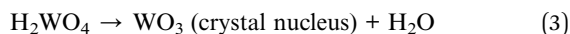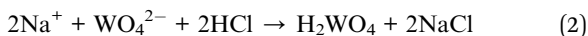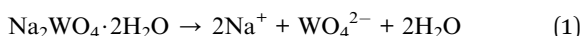

Fig. 1 The SEM images of WO$_3$-X prepared at different pH (a) 1.6; (b) 1.8; (c) 2.0; (d) high magnification SEM images at 2.0 pH; (e) 2.5 and (f) 3.0 of the various morphologies.

nanorods. The growth mechanism of the different morphologies WO$_3$-X can be explained according to the following reactions:[30]

$$Na_2WO_4 \cdot 2H_2O \rightarrow 2Na^+ + WO_4^{2-} + 2H_2O \qquad (1)$$

$$2Na^+ + WO_4^{2-} + 2HCl \rightarrow H_2WO_4 + 2NaCl \qquad (2)$$

$$H_2WO_4 \rightarrow WO_3 \text{ (crystal nucleus)} + H_2O \qquad (3)$$

$$WO_3 \text{ (crystal nucleus)} \rightarrow WO_3 \text{ (different morphologies)} \qquad (4)$$

A certain amount of water was added to Na$_2$WO$_4$ salt to form 2Na$^+$ and WO$_4^{2-}$ ions and then HCl was added dropwise (pH = 3) resulting in the formation of H$_2$WO$_4$. H$_2$WO$_4$ (yellowish transparent tungstic acid) was transferred to the reactor and heated until 180 °C for 24 h. Nucleation was started and WO$_3$ crystal nuclei were obtained when the reaction temperature exceeded the decomposition temperature of H$_2$WO$_4$, and then different pH solutions resulted in the formation of different morphologies of WO$_3$.

The phase structures of WO$_3$-X samples were examined using XRD (Fig. 2a). All the diffraction peaks were well indexed to the pure hexagonal phase structure of WO$_3$ (JCPDS card no. 33-1387) and no characteristic peaks from impurities can be detected. The strong diffraction peaks at 2θ angle of 13.9, 22.7, 28.2 and 36.6° can be clearly assigned to the (100), (001), (200) and (201) planes of WO$_3$, respectively. The average crystallite size of the material was calculated using the Scherrer equation:

$$D = K\lambda/\beta \cos \theta \qquad (5)$$

where λ is the X-ray wavelength, β is the full width at half maximum, and θ is the diffraction angle. The average crystallite size was found to be 117.3 nm. These sharp and intense peaks in XRD patterns imply some differences in crystallite size and microstructure of WO$_3$ samples and display good crystallinity of WO$_3$ synthesized at different pH. The chemical composition and valence state of the WO$_3$-2.0 was analysed using the XPS technique and the peaks at the binding energy corresponding to tungsten and oxygen were detected (Fig. 2b). The curves of tungsten can be fitted to four spin–orbit doublets as exhibited in Fig. 2c, the W 4f photoelectron core-level spectra can be assigned to W 4f$_{5/2}$ and W 4f$_{7/2}$ with the interval of 2.13 eV.[31] The curves were divided into four peaks attributed to W^{6+} and W^{5+} states, implying the existence of W^{6+} and W^{5+} in WO$_3$-2.0. The peaks located at binding energies of 35.73 eV and 37.86 eV are attributed to W^{6+} state, while the peaks at 36.01 eV and 38.26 eV are attributed to W^{5+}. The intensity of W^{6+} is stronger than that of the W^{5+}, indicating that WO$_3$-2.0 is mainly in the form of W^{6+}.[32] The energy-dispersive X-ray spectroscopy (EDS) and corresponding mapping images were further analyzed to obtain the elemental distribution characteristics that are shown in Fig. 2d. The homogeneous distribution of tungsten and oxygen in nanomaterials can be unambiguously confirmed from the corresponding mapping images.

The obtained different morphologies and structures WO$_3$-X nanosheets were firstly investigated as electrodes for supercapacitors in a three-electrode cell using 1 M H$_2$SO$_4$ as the aqueous electrolyte. Fig. 3a exhibits the GCD curves of the WO$_3$-X nanosheets as the electrode at 0.5 A g^{-1} in the potential window of −0.65–0.2 V. Obviously, the WO$_3$-2.0 nanosheets exhibit a high specific capacitance of 98.1 mA h g^{-1}, the value

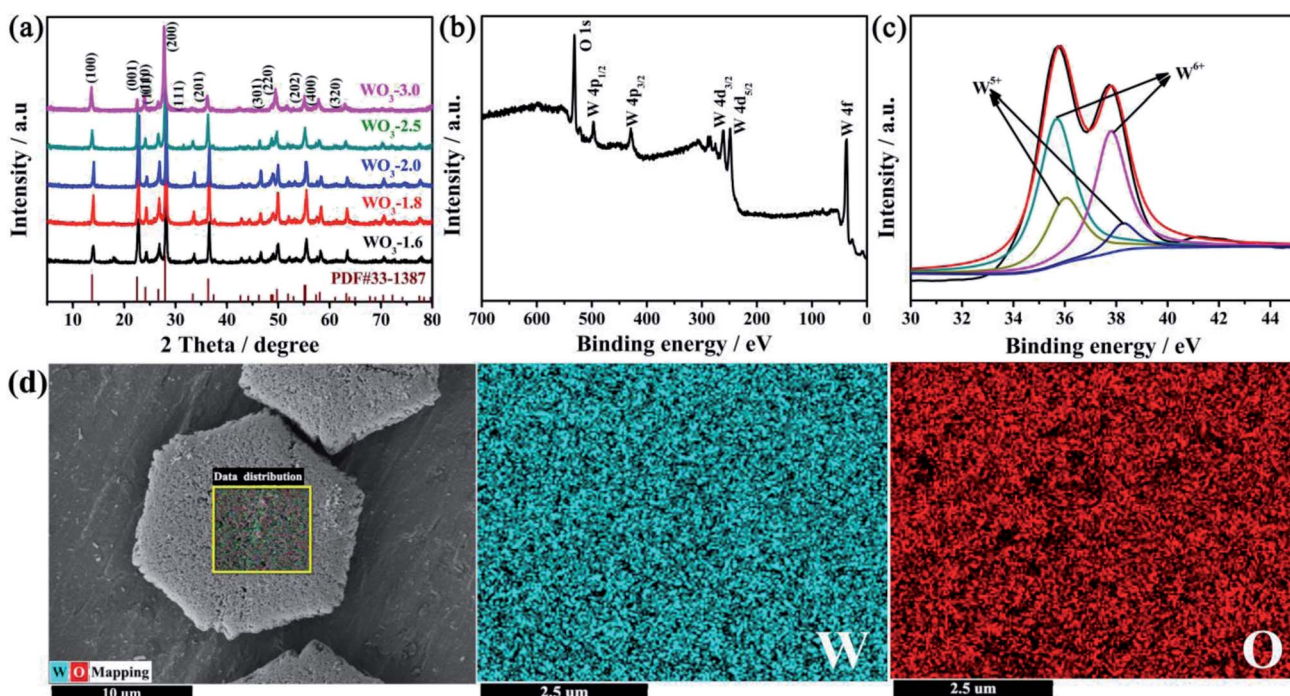Fig. 2 (a) XRD patterns; (b) XPS survey spectra and (c) high-resolution XPS spectra of W 4f peak of WO$_3$-2.0; (d) SEM image of WO$_3$-2.0 and the corresponding element mapping images (selected from the square region) for the tungsten and oxygen.
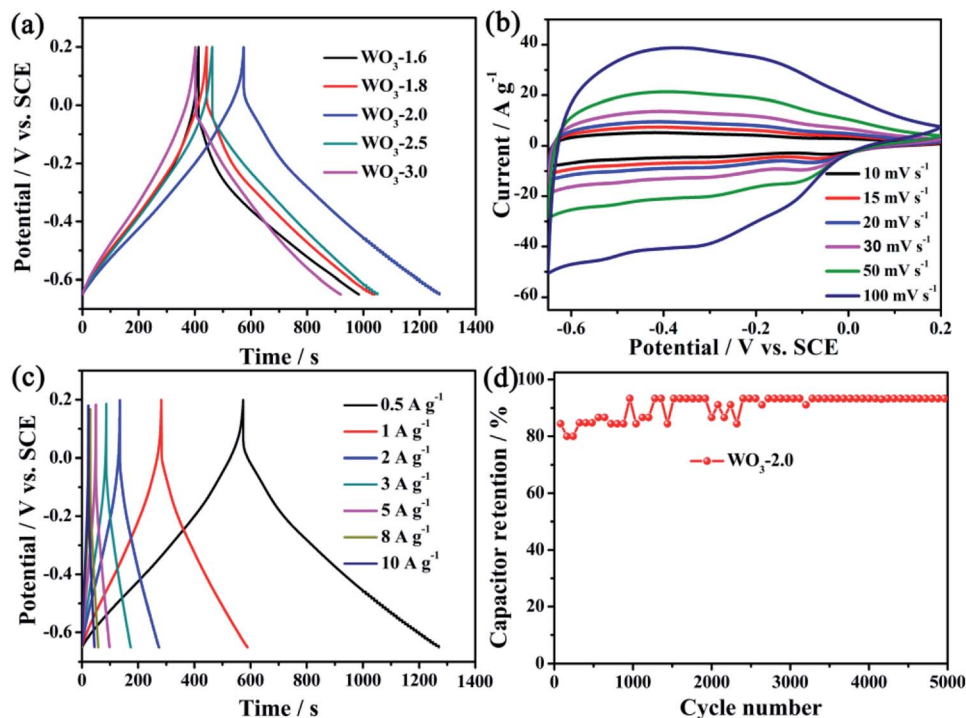
Fig. 3 (a) GCD curves of WO_3-X different sample at the current density of 0.5 A g^{-1}; (b) CV curves of WO_3-2 at various scan rates; (c) GCD curves of WO_3-2 at different current densities; (d) cycling performances of WO_3-2.0 negative electrode material at the current density of 2 A g^{-1}.

that is higher than that of other WO_3-X nanomaterials. As can be displayed in Fig. 3b, the characteristic redox peaks of the electrode are observed, indicating that it has typical faradaic pseudocapacitance behavior. The redox peak in the electrochemical performance measurement is attributed to sulfuric acid as the electrolyte, which occurs in the WO_3 block and the reversible intercalation/deintercalation of H^+ ions at the interface between WO_3 and the electrolyte. The electrochemical mechanism of WO_3 in H_2SO_4 electrolyte can be expressed as: $WO_3 + xe^- + xH^+ \leftrightarrow H_xWO_3$.[33] Moreover, with the increase in sweep speed, the shape of CV curves remains linear without any change, showing excellent electrochemical behavior. Fig. 3c shows GCD curves of WO_3-2.0 electrodes at various current densities from 0.5 to 10 A g^{-1}. The specific capacitance of the electrodes can be calculated using the above-mentioned formula. The gravimetric capacitances of WO_3-2.0 at different current densities 0.5 to 10 A g^{-1} are found to be 98.1, 85.8, 77.7, 73.2, 67.8, 63.8, 61.1 and 56.7 mA h g^{-1}, respectively, showing excellent electrochemical performance.[34] In order to further evaluate the cycle stability of the WO_3-2.0 electrode was subjected to a GCD cycle at 2 A g^{-1}. The electrochemical impedance spectroscopy (EIS) measurements of all electrodes recorded in the open circuit potential are shown in Fig. S2.† By comparison, it is found that the WO_3-2.0 electrode has the smallest resistance (R_s = 3.227 Ω, R_{ct} = 3.923 Ω), which indicates that the WO_3-2.0 electrode has efficient charge transfer. As presented in Fig. 3d, it can be seen that the specific capacitance increases clearly before the initial 1000 cycles, which may be due to the improvement of the electrode surface wettability during the initial charge/discharge process. Subsequently, the specific

capacitance decreases slightly and remained at about 93.3% of the maximum capacitance after 5000 cycles, indicating that the WO_3-2.0 electrode material has outstanding electrochemical reversibility and stability in aqueous H_2SO_4 electrolyte.

3.2.   Characterizations of APAC-2-positive electrode materials

The synergistic effect between the large surface area and good electrical conductivity of the electrode material may have a major effect on improving the capacitance of the supercapacitor. *Via* an effective simultaneous activation-graphitization (SAG) route from alfalfa, we can easily obtain high yield and inexpensive graphite-like porous carbon materials. The shape and size characteristics of the carbon were analyzed using FE-SEM. Fig. 4 shows an SEM image with different degrees of carbonation. The carbon only added $FeCl_3$ as graphitized precursor after carbonization shows a pleated smooth surface (Fig. 4a). However, when $ZnCl_2$ was used as the activation agent with $FeCl_3$ at the same temperature (Fig. 4b), some irregular pores on the macroscopic scale could be observed on the rough surface. As shown in Fig. 4c, with an increase of $ZnCl_2$ content, APAC-2 has a number of irregular pores on the rough surface and also appears loose with less agglomeration than APAC-1. The shape and size of APAC-2 might make ionic diffusion from the electrolyte into the inner space of carbon materials easier. When alfalfa and $ZnCl_2$ mass rations reached 1 : 3 (Fig. 4d), the surface of APAC-3 became smooth and the original macroscopic pores disappeared, possibly due to cracking of the pores during pyrolysis.
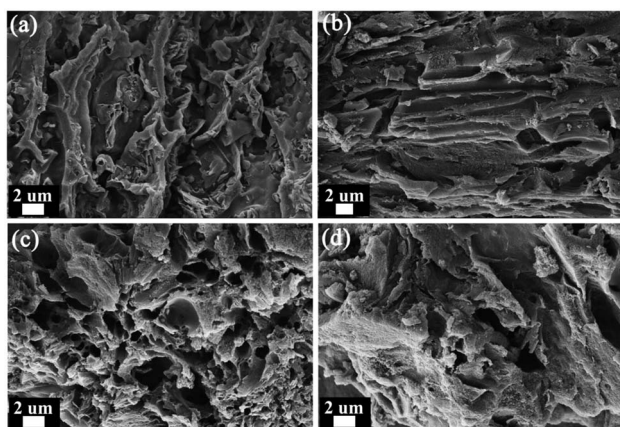
Fig. 4 SEM of the samples: (a) APAC-0; (b) APAC-1; (c) APAC-2; (d) APAC-3.

X-ray diffraction (XRD) analysis was used to survey the APAC-2 structure as shown in Fig. 5a. The diffraction peak at a 2θ value of $23.7°$ can be assigned as the (002) reflection of ordered graphite sheets, and sharp peaks at $42.5°$ are indexed to the (100) plane of standard graphene. Both diffraction peaks are present in width and low intensity in the height of the 100 and 002 planes, suggesting high crystallinity of the APAC-2 sample. The graphite property of APAC-2 was further demonstrated by Raman spectroscopy as presented in Fig. 5b. The peaks at 1343 cm^{-1} and 1592 cm^{-1} corresponding to the D band are related to the defects (or disorder structures) and the G band is related to the first-order scattering of the E_{2g} mode observed for sp²-carbon domains of the carbon material, respectively.[35,36] Moreover, the relative intensity of the D to G band (I_D/I_G) is proportional to the number of carbon defect sites and is used to study the degree of disorder in the graphitic structure. In other words, the higher the proportion, the lower the degree of graphitization. For APAC-2, the I_D/I_G ratio was 0.95, it is indicated that the APAC-2 carbon materials have a higher graphitization degree and less disordered structure.[37] These XRD and Raman analyses further suggest that APAC-2 possesses a portion of the graphitized structure that may lead to its good electronic conductivity.

In order to investigate the development of porosity *via* $ZnCl_2$ and $FeCl_3$ activation, the specific surface area and the pore structure of the activated carbon samples were measured by N_2 adsorption–desorption technique. According to the isotherm of the samples (Fig. 5c), APAC-0 has a typical I-type curve with nonporous characteristics, but APAC-1, APAC-2 and APAC-3 show typical type IV curves with clear H_2-type hysteresis loop, which are characteristic of mesoporous materials based on the IUPAC classification. On the other hand, with the increased mass ratio of alfalfa to $ZnCl_2$, the sharply increased adsorption volumes show a much more developed porous structure. It is implied that the activated carbon samples (APAC-1, APAC-2, and APAC-3) contain the coexistence of micropores and mesopores at relative pressures from 0 to 0.9. The pore size distribution (Fig. 5d) is calculated by the nonlocal density functional theory (NLDFT) method based on the adsorption branch of the isotherm. Table 1 summarizes the specific surface area, pore volume and average pore size of APACs obtained from BET
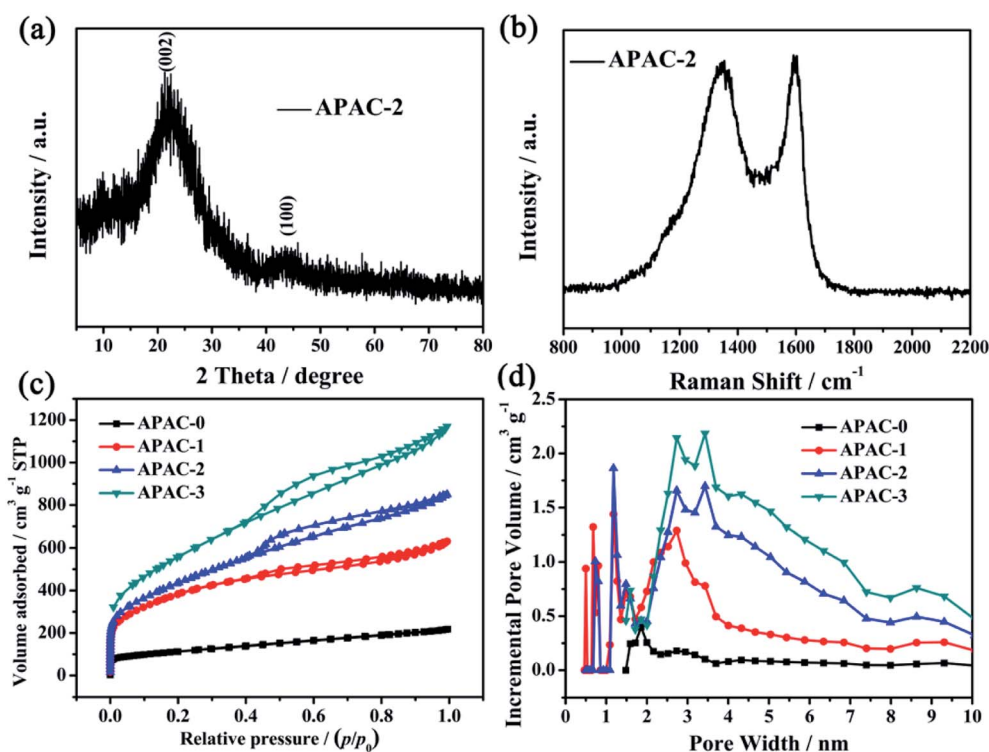

Fig. 5 (a) XRD patterns; (b) Raman spectrum; (c) nitrogen adsorption–desorption isotherms and (d) pore size distributions of the as-prepared carbons.

Table 1 BET surface area and pore structure characterization parameters of APACs

| Samples	$S_{BET}{}^a$ (m^2 g^{-1})	$V_{total}{}^b$ (cm^3 g^{-1})	D^c (nm)
APAC-0	381.2	0.265	2.322
APAC-1	1322.5	0.542	2.863
APAC-2	1576.3	0.755	3.336
APAC-3	2037.6	0.832	3.552

^{a} Specific surface area determined according to BET (Brunauer–Emmett–Teller) method. ^{b} Total pore volume at $P/P_0 = 0.99$. ^{c} Adsorption average pore diameter.

measurements. The results reveal that the porosity of the samples mainly results from micropores (<2 nm) and mesopores (2–5 nm), the NLDFT pore size distribution indicates that APAC-2 exhibits a porous structure that is mainly made up of micropores (1.3 nm) and mesopores (2.3 nm). The high specific surface area and a large number of pores of APAC-2 provide plentiful ions adsorption sites and a high density of interconnected ions-diffusion channels, which facilitate electrolyte ions transport in APAC-2 electrode materials.

XPS analysis was used to further study the chemical composition in APAC-2. As shown in Fig. 6a. It shows a predominant C 1s peak at around 298.2 eV, weak O 1s peak near 544.8 eV, and N 1s peak at about 412.2 eV. In addition, other impurities were not detected in the range of 200–800 eV, suggesting a high purity of the prepared carbon APAC-2.
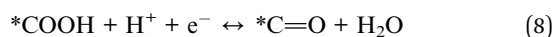
Obviously, the C 1s spectrum of APAC-2 can be fitted by four different binding states: C=C (284.5 eV), C–N/C–O–R (285.5 eV), and apparent C=N/C=O (286.4 eV) bonds,[38] which clearly reveal that the nitrogen and oxygen atoms have been doped in the structure. The peak deconvolution of the N 1s spectrum reveals the presence of N-6 pyridinic (398.4 eV), N-5 pyrrolic/pyridone (400.5 eV), N–Q quaternary (401.5 eV) and pyridine N-oxide (402.7 eV),[38,39] as shown in Fig. 6c. According to previous reports, N–Q can significantly increase the electrical conductivity of carbon materials, and N-5 and N-6 may produce a large number of external defects and active sites, which are facilitating the rapid diffusion of transport ions and produce pseudocapacitance.[40] The O 1s core-level spectrum (Fig. 6d) can be deconvoluted into three different components attributed to C=O in ketone/carbonyl (530.9 eV), O–C in lactone, phenol/ether/epoxy (532.5 eV), and C=O in carboxylic acid (534.0 eV).[41] The presence of C=O and C–O groups is very important for wettability with the aqueous electrolyte, resulting in an effective charge storage area. The carbon materials that contain N and O atoms not only considerably contribute to improving wettability but also increase the number of chemically reactive sites and improve the holistic specific capacitance.[14]

In order to further explore the potential application of APACs as electrodes for supercapacitors, their electrochemical behavior have been analyzed in a standard three-electrode system within a potential window of 0–1.0 V. Fig. 7a displays the GCD curve of APAC electrodes at a current density of 0.5 A g^{-1}. The specific
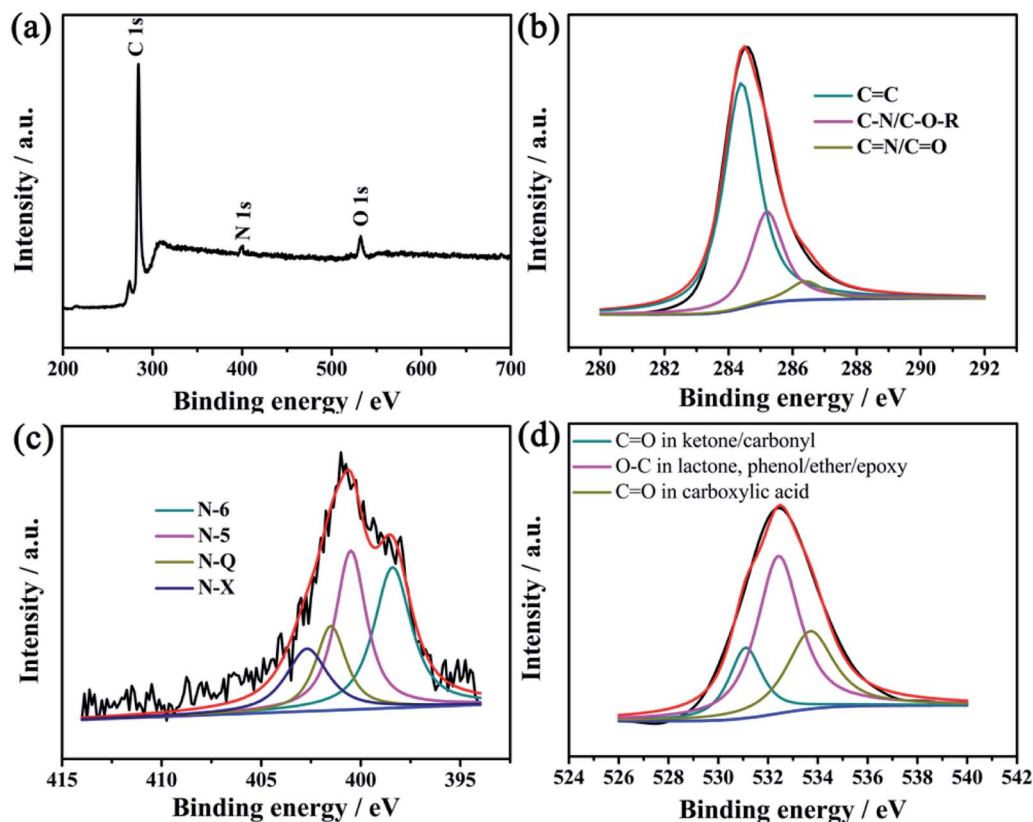
Fig. 6 (a) XPS survey spectra and (b–d) high-resolution XPS spectra of the deconvoluted C 1s, N 1s and O 1s peak of APAC-2.

capacitance APAC-0, APAC-1, APAC-2, and APAC-3 are 154.1, 207.9, 262.1, and 188.7 F g^{-1}, respectively. Typically, the APAC-2 sample exhibits the utmost charge/discharge time, indicating that the APAC-2 sample has a higher specific capacitance than others because the electrolyte ions have sufficient time to enter and diffuse into the porosity at lower current densities. Cyclic voltammetry (CV) is a powerful technique for the determination of redox potentials and involved electron transfer redox reactions. As can be seen from Fig. 7b, there is a small oxidation-reduction peak observed in two samples of CVs 0.3–0.4 V, which might be due to the effect of the quinone functional group on the Faraday pseudocapacitance.[42] The pseudocapacitance of APAC electrodes could be caused by the reversible reactions between different types of oxygen-containing functional groups, which on the surface of carbon materials produce pseudocapacitance and increased surface area after activation, enhancing the electric double-layer capacitance. The process is described through the following reactions:[43]

$$*C–OH + H^+ + e^- \leftrightarrow *C + H_2O \tag{6}$$

$$*C=O + H^+ + e^- \leftrightarrow *C + OH \tag{7}$$

$$*COOH + H^+ + e^- \leftrightarrow *C=O + H_2O \tag{8}$$

As shown in Fig. 7b, the shape of CV curves remained similar even though the scan rate is up to 100 mV s^{-1}, implying the good rate capability of the APAC-2 electrode. The GCD curve of the APAC-2 (Fig. 7c) at various current densities still maintains a curved shape. It shows that the higher specific capacitances are 262.1 F g^{-1} at 0.5 A g^{-1} (184 F g^{-1} even at 10 A g^{-1}), which indicates excellent capacitive behavior and electrochemical reversibility. In order to objectively highlight the superiority of APAC-2, we compared the electrochemical properties of different carbon-based electrode materials reported in the literature previously, as listed in Table S1.† Fig. S3† presents the Nyquist plot of the APAC-2 sample. The low resistance values ($R_s = 0.92$ Ω, $R_{ct} = 0.07$ Ω) reveal that the APAC-2 sample possesses excellent capacitive behavior. In addition, cycling stability is also a crucial parameter for supercapacitors electrode materials. To survey the cycling stability, the GCD cycling of the APAC-2 was performed at 2 A g^{-1} (Fig. 7d). After 5000 cycles, the capacity decay was only 4% compared with the starting value, which indicates that the as-synthesized activated carbon electrode is a promising candidate in long-term energy storage devices.

3.3. Electrochemical behavior of the asymmetric supercapacitor

Based on the electrode characteristics of the carbon material APAC-2 and WO$_3$-2.0, a novel asymmetric supercapacitor (ASC) was fabricated by using these two different materials as positive and negative electrodes, respectively. The WO$_3$-2.0 nanorod bundle electrode was measured in a potential window of −0.65–0.2 V (vs. SCE), while the APAC-2 electrode was measured in a potential window of 0 to 1 V (vs. SCE) in 1 M H$_2$SO$_4$ electrolyte, as shown in Fig. 8a. Consequently, the cell voltage can be
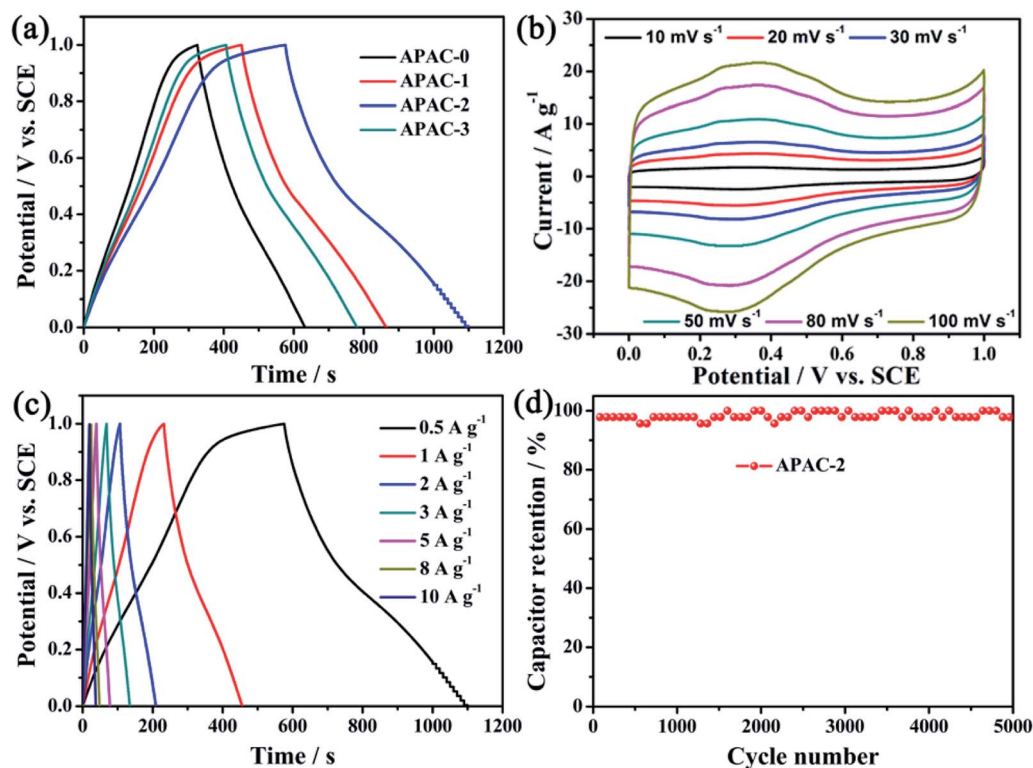

Fig. 7 (a) GCD curves of APACs different sample at the current density of 0.5 A g^{-1}; (b) CV curves of APAC-2 at various scan rates; (c) GCD curves of APAC-2 at different current densities; (d) cycling performances of APAC-2 positive electrode material at the current density of 2 A g^{-1}.

expressed as the sum of the potential range of the positive and negative electrodes, it can be extended up to approximately 1.65 V when assembled into ASC.[44] However, to ensure the stability of the two-electrode cell, the ASC (APAC-2//WO₃-2.0) operating unit voltage was optimized from 0 to 1.6 V (Fig. 8b). It is necessary to maintain a balance between positive and negative charges to balance the charge balance in asymmetric supercapacitors, based on the following formula:[45]

$$Q = C_m \times \Delta V \times m \tag{9}$$

where Q (C) refers to stored charges, C_m (F g^{-1}) represents the specific capacitance, ΔV (V) is the potential change, and m (g) corresponds to the total weight of the carbon APAC-2 and WO₃-2.0. In order to obtain $q^+ = q^-$, and with the largest voltage window. According to the above study, we chose the specific

capacitance values and potential range of the carbon material APAC-2 and the WO₃-2.0 electrode at a current density of 1 A g^{-1}, the mass balance will be expressed as the following equation:

$$m^+/m^- = (C_m^+ \times \Delta V^+)/(C_m^- \times \Delta V^-) \tag{10}$$

The CV curves of the APAC-2//WO₃-2.0 ASC device is shown in Fig. 8b, which still exhibit distorted semi-rectangular-shaped CV curves with obvious two pairs of redox peaks in the operating voltage of 1.6 V even at 100 mV s^{-1}, implying a faradaic pseudocapacitance charge/discharge rate process over the entire voltammetric cycle and an ideal fast charge/discharge performance.[46] At lower scan rates, ions can be effectively diffused into the active sites. At higher scan rates, ions may only be
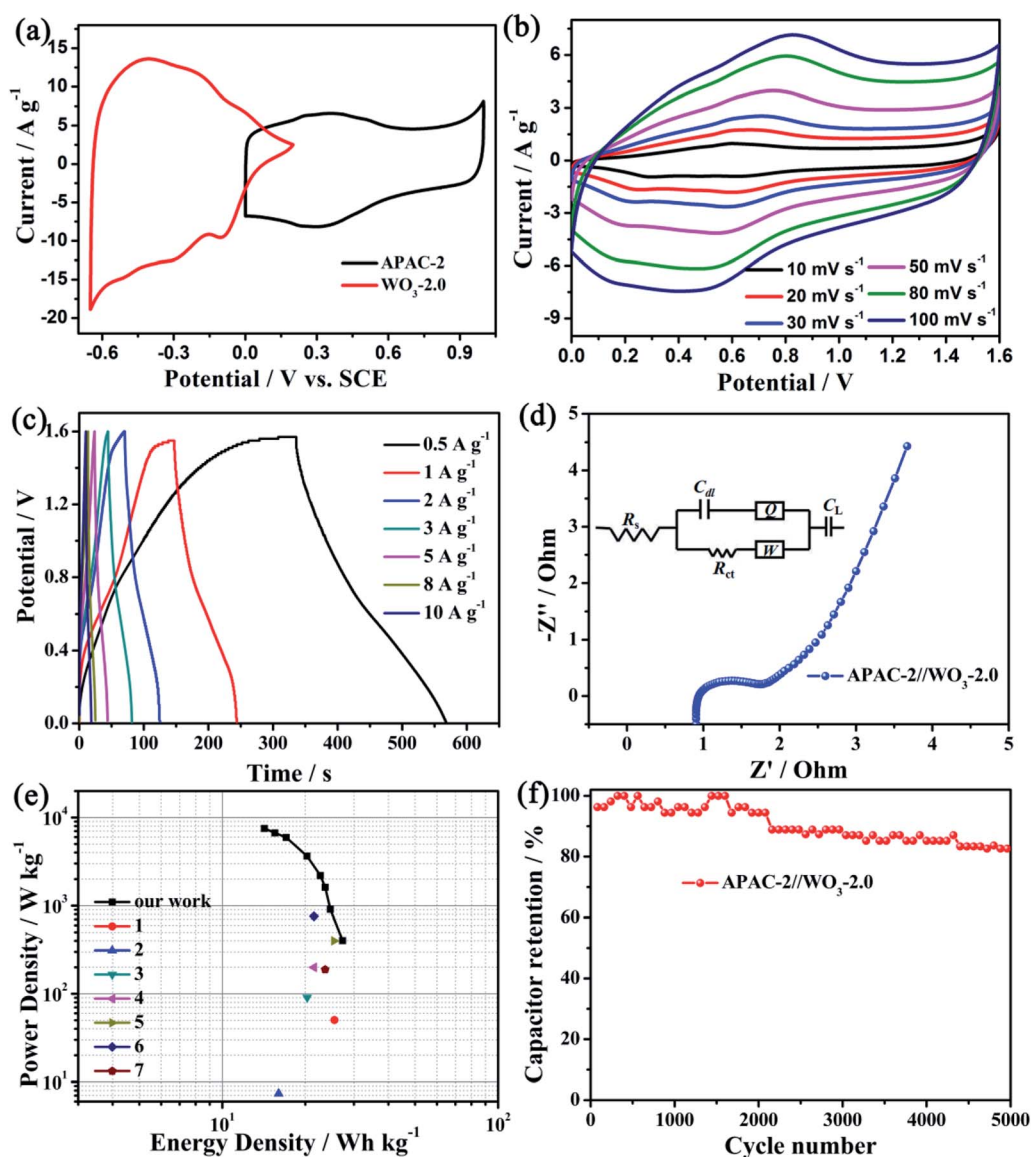
Fig. 8 (a) CV curves of the APAC-2 and WO₃-2.0 electrodes in a three-electrode cell at 30 mV s^{-1} in 1 M H₂SO₄; (b) CV curves of the ASC at various scan rates; (c) GCD curves of the ASC at various current densities; (d) Nyquist plot of the ASC (inset of the equivalent circuit model); (e) Ragone plots related to energy and power densities plot and (f) cycling stability of the APAC-2//WO₃-2.0 ASC in a two electrode cell.

Table 2 The electrochemical properties of different ASCs

Electrode		Device performance			
Positive	Negative	Energy density (W h kg^{-1})	Power density (kW kg^{-1})	Number	Ref.
MnO$_2$ NWs@SWNTs	In$_2$O$_3$ NWs@SWNTs	25.5	50.3	1	49
MnO$_2$@rGO	Ppy@rGO	16	7.4	2	50
AC	Co(OH)$_2$	20.3	90.6	3	51
Cu$_{1.79}$Co$_{0.21}$CH/NF	Graphene/NF	21.5	200	4	52
CNT@NiO	PCPs	25.4	400	5	53
MCMSs	RGO	21.5	759	6	54
MnO$_2$@CCNs	CCNs	23.6	188.8	7	55
APAC-2	WO$_3$-2.0	27.3	403.1	Our work	

immersed in the surface of the substance. Since the lower scanning rate is provided for a longer time, the active site interacts better with the ions, showing a good rate capability for the electrode of a supercapacitor.[47] The highly symmetrical GCD curves of APAC-2//WO$_3$-2.0 ASC at various current densities from 0.5 to 10 A g^{-1} (Fig. 8c) are indicative of excellent capacitive behavior and electrochemical reversibility. To better study the ion transport properties of the APAC-2//WO$_3$-2.0 ASC, electrochemical impedance spectroscopy (EIS) test was carried out over the frequency range from 0.1 Hz to 100 kHz, as shown in Fig. 8d. The Nyquist plot includes a linear part in the low-frequency region, with a small semicircle frequency region at high places, indicating a significant capacitive behavior and a low charge transfer resistance, respectively. The data of EIS can be well-matched with the equivalent circuit shown in the inset of Fig. 8d, the intercept at the real axis (Z') of the plot provides the equivalent series resistance (R_s), which includes the bulk resistance of the electrolyte and the contact resistance at the interface between the electrolyte and electrode as well as the intrinsic resistance of the electroactive materials. R_{ct} is generated by the reaction of a faradaic and electronic double-layer capacitor (C_{dl}) at the interface between the electrode and electrolyte.[48] The 45° inclined curve in the middle frequencies is the Warburg impedance (Z_W), which is a result of the frequency dependence of ion diffusion/transport in electrolytes. It is worth noting that, as seen from Fig. 8d, the APAC-2//WO$_3$-2.0 electrode not only displays a small R_{ct} (0.74 Ω) but also shows a small R_s (0.93 Ω), showing that ASC has a rapid charge transfer process. The Ragone plot of the APAC-2//WO$_3$-2.0 ASC device is obtained on the basis of the GCD data, as given in Fig. 8e. It is obvious that the APAC-2//WO$_3$-2.0 ASC shows the energy density of 27.3 W h kg^{-1} at a power density of 403.1 W kg^{-1} and it still maintains an energy density of 14.2 W h kg^{-1} at a power density of 7529.4 W kg^{-1}. The maximum energy density obtained from APAC-2//WO$_3$-2.0 ASC is much higher than the symmetrical and asymmetrical supercapacitors in the previous report, as displayed in Fig. 8e and Table 2.

The cycling stability is also a crucial parameter for supercapacitors. The long-term stability of the APAC-2//WO$_3$-2.0 ASC was examined by GCD cycling at a current density of 2 A g^{-1}, as shown in Fig. 8f. In the previous 2000 cycles, the electrode material was unstable, however, after 5000 cycles, the specific

capacitance of the ASC can be maintained to 82.6%, which indicates that the ASC exhibits excellent electrochemical stability. It exhibits good cycling stability, which may be due to the porosity of the carbon material and good electrochemical performance of WO$_3$-2.0 during the charge–discharge process, this result makes it a promising candidate for long-term energy storage devices.

4. Conclusions

The morphology, crystallinity and electrochemical properties of WO$_3$-X are mainly affected by H in the hydrothermal reaction. WO$_3$-2.0 has inerratic hexagonal-like morphology, and possesses the highest specific capacitance of 98.1 mA h g^{-1} at 0.5 A g^{-1}. By following a simple and cost-effective method, porous activated carbon using alfalfa as raw material was also prepared. APAC-2 has a 3D porous structure, large surface area (1576.3 m^2 g^{-1}), high specific capacitance (262.1 F g^{-1} at 0.5 A g^{-1}), good cycling stability with 96% of initial specific capacitance after 5000 cycles. The APAC-2//WO$_3$-2.0 aqueous asymmetric supercapacitor (ASC) in 1 M H$_2$SO$_4$ electrolyte with high energy density was assembled on the basis of an inerratic hexagonal-like WO$_3$-2.0 nanorod bundle as a negative electrode and graphene-like nanosheet porous activated carbon (APAC-2) agricultural alfalfa as a positive electrode. The assembled ASC showed a high energy density of 27.3 W h kg^{-1} at a power density of 403.1 W kg^{-1} with an output voltage of 1.6 V, good cycling stability with 82.6% specific capacitance remaining after 5000 cycles. The synthesis strategy in this work can open up a new approach to the development of advanced energy materials based on alkali metal tungsten trioxide and renewable biomass wastes for the preparation of porous carbon.

Conflicts of interest

There are no conflicts to declare.

Acknowledgements

References

1 N. Choudhary, C. Li, J. Moore, N. Nagaiah, L. Zhai, Y. Jung and J. Thomas, Supercapacitors: Asymmetric Supercapacitor Electrodes and Devices, *Adv. Mater.*, 2017, **29**, 1605336.

2 M. Gidwani, A. Bhagwani and N. Rohra, Supercapacitors: the near future of batteries, *Int. J. Eng. Inventions*, 2014, **4**, 22–27.

3 B. Scrosati, J. Hassoun and Y. K. Sun, Lithium-ion batteries. A look into the future, *Energy Environ. Sci.*, 2011, **4**, 3287–3295.

4 C. Liu, F. Li, L.-P. Ma and H. M. Cheng, Advanced materials for energy storage, *Adv. Mater.*, 2010, **22**, 28.

5 M. Winter and R. J. Brodd, What are batteries, fuel cells, and supercapacitors, *Chem. Rev.*, 2004, **104**, 4245–4270.

6 B. E. Conway, *Electrochemical Supercapacitors: Scientific Fundamentals, Technological Applications*, Springer Sci. Business Media, 2013.

7 Z. L. Wang, Piezopotential Gated Nanowire Devices: Piezotronics and Piezo-Phototronics, *Nano Today*, 2010, **5**, 540–552.

8 P. Simon and Y. Gogotsi, Materials for Electrochemical Capacitors, *Nat. Mater.*, 2008, **7**, 845–854.

9 J. Kondoh, I. Ishii, H. Yamaguchi, A. Murata, K. Otani, K. Sakuta, N. Higuchi, S. Sekine and M. Kamimoto, Electrical energy storage systems for energy networks, *Energy Convers. Manage.*, 2000, **41**, 1863–1874.

10 V. Augustyn, P. Simon and B. Dunn, Pseudocapacitive oxide materials for high-rate electrochemical energy storage, *Energy Environ. Sci.*, 2014, **7**, 1597–1614.

11 P. C. Chen, G. Shen, Y. Shi, H. Chen and C. Zhou, Preparation and characterization of flexible asymmetric supercapacitors based on transition-metal-oxide nanowire/single-walled carbon nanotube hybrid thin-film electrodes, *ACS Nano*, 2010, **4**, 4403–4411.

12 S. K. Balasingam, J. S. Lee and Y. Jun, Few-layered MoSe$_2$ nanosheets as an advanced electrode material for supercapacitors, *Dalton Trans.*, 2015, **44**, 15491–15498.

13 H. Pang, X. Li, Q. Zhao, H. Xue, W. Y. Lai, Z. Hu and W. Huang, One-pot synthesis of heterogeneous Co$_3$O$_4$-nanocube/Co(OH)$_2$-nanosheet hybrids for high-performance flexible asymmetric all-solid-state supercapacitors, *Nano Energy*, 2017, **35**, 138–145.

14 M. A. Borysiewicz, M. Ekielski, Z. Ogorzałek, M. Wzorek, J. Kaczmarski and T. Wojciechowski, Highly transparent supercapacitors based on ZnO/MnO$_2$ nanostructures, *Nanoscale*, 2017, **9**, 7577–7587.

15 X. Lu, T. Zhai, X. Zhang, Y. Shen, L. Yuan, B. Hu, L. Gong, J. Chen, Y. Gao, J. Zhou, Y. Tong and Z. L. Wang, WO$_3$-x@Au@MnO$_2$ core–shell nanowires on carbon fabric for high-performance flexible supercapacitors, *Adv. Mater.*, 2012, **24**, 938–944.

16 C. Jo, J. Wang, H. Song, A. H. Dao, Y.-T. Kim, S. H. Lee, S. W. Hong, S. Yoon and J. Lee, Capacitors: Block Copolymer Assisted One Pot Synthesis of Ordered Mesoporous WO$_3$-x/Carbon Nanocomposites as High-Rate-Performance Electrodes for Pseudocapacitors, *Adv. Funct. Mater.*, 2013, **23**, 3713.

17 W. Su, L. Zhou and Y. P. Zhou, Preparation of microporous activated carbon from coconut shells without activating agents, *Carbon*, 2003, **41**, 861–863.

18 G. Ma, F. Hua, K. Sun, Z. Zhang, E. Feng, H. Peng and Z. Lei, Porous carbon derived from sorghum stalk for symmetric supercapacitor, *RSC Adv.*, 2016, **6**, 103508–103516.

19 F. Gao, J. Qu, Z. Zhao, Z. Wang and J. Qiu, Nitrogen-doped activated carbon derived from prawn shells for high-performance supercapacitors, *Electrochim. Acta*, 2016, **190**, 1134–1141.

20 L. Sun, C. Tian, M. Li, X. Meng, L. Wang, R. Wang, J. Yin and H. Fu, From coconut shell to porous graphene-like nanosheets for high-power supercapacitors, *J. Mater. Chem. A*, 2013, **1**, 6462–6470.

21 C. Long, X. Chen, L. Jiang, L. Zhi and Z. Fan, Porous layer-stacking carbon derived from in-built template in biomass for high volumetric performance supercapacitors, *Nano Energy*, 2015, **12**, 141–151.

22 A. Burke, Ultracapacitors: why, how, and where is the technology, *J. Power Sources*, 2000, **91**, 37–50.

23 P. J. Hall and E. J. Bain, Energy-storage technologies and electricity generation, *Energy Policy*, 2008, **36**, 4352–4355.

24 I. Hadjipaschalis, A. Poullikkas and V. Efthimiou, Overview of current and future energy storage technologies for electric power applications, *Renew. Sustain. Energy Rev.*, 2009, **13**, 1513–1522.

25 Y. Zhao, L. Hu, S. Zhao and L. Wu, Preparation of MnCo$_2$O$_4$@Ni(OH)$_2$ Core–Shell Flowers for Asymmetric Supercapacitor Materials with Ultrahigh Specific Capacitance, *Adv. Funct. Mater.*, 2016, **26**, 4085–4093.

26 R. D. Kumar, Y. Andou and S. Karuppuchamy, Facile synthesis of Co–WO$_3$/functionalized carbon nanotube nanocomposites for supercapacitor applications, *J. Mater. Sci. Mater. Electron.*, 2017, **28**, 5425–5434.

27 M. Qiu, P. Sun, L. Shen, K. Wang, S. Song, X. Yu, S. Tan, C. Zhao and W. Mai, WO$_3$ nanoflowers with excellent pseudo-capacitive performance and the capacitance contribution analysis, *J. Mater. Chem. A*, 2016, **4**, 7266–7273.

28 Z. Pan, Y. Qiu, J. Yang, F. Ye, Y. Xu, X. Zhang, M. Liu and Y. Zhang, Ultra-endurance flexible all-solid-state asymmetric supercapacitors based on three-dimensionally coated MnOx nanosheets on nanoporous current collectors, *Nano Energy*, 2016, **26**, 610–619.

29 X. Tang, Y. Lui, A. Merhi, B. Chen, S. Ding, B. Zhang and S. Hu, Redox-active hydrogel polymer electrolytes with different pH values for enhancing the energy density of the hybrid solid-state supercapacitor, *ACS Appl. Mater. Interfaces*, 2017, **9**, 44429–44440.

30 G. Cai, J. Tu, D. Zhou, L. Li, J. Zhang, X. Wang and C. Gu, The direct growth of a WO$_3$ nanosheet array on a transparent conducting substrate for highly efficient electrochromic and electrocatalytic applications, *Crystengcomm*, 2014, **16**, 6866–6872.

31 J. Wang, E. Khoo, P. S. Lee and J. Ma, Synthesis, Assembly, and Electrochromic Properties of Uniform Crystalline WO$_3$ Nanorods, *J. Phys. Chem. C*, 2008, **112**, 14306–14312.

32 C. Navio, S. Vallejos, T. Stoycheva, E. Llobet, X. Correig, R. Snyders, C. Blackman, P. Umek, X. Ke, G. V. Tendeloo and C. Bittencourt, Gold clusters on WO$_3$ nanoneedles grown via AACVD: XPS and TEM studies, *Mater. Chem. Phys.*, 2012, **134**, 809–813.

33 P. A. Shinde, A. C. Lokhande, N. R. Chodankar, A. M. Patil, J. H. Kim and C. D. Lokhande, Temperature dependent surface morphological modifications of hexagonal WO$_3$ thin films for high performance supercapacitor application, *Electrochim. Acta*, 2017, **224**, 397–404.

34 A. Y. Gokhshtein, *Poverkhnostnoe Natyazhenie Tverdykh Tel I Adsorbtsiya (The Surface Stress in Solids and the Adsorption)*, Nauka Moscow (in Russian), 1976.

35 Z. Fan, J. Yan, T. Wei, L. Zhi, G. Ning, T. Li and F. Wei, Asymmetric Supercapacitors Based on Graphene/MnO$_2$ and Activated Carbon Nanofiber Electrodes with High Power and Energy Density, *Adv. Funct. Mater.*, 2011, **21**, 2366–2375.

36 S. Gao, K. Geng, H. Liu, X. Wei, M. Zhang, P. Wang and J. Wang, Transforming organic-rich amaranthus waste into nitrogen-doped carbon with superior performance of the oxygen reduction reaction, *Energy Environ. Sci.*, 2015, **8**, 221–229.

37 A. Sadezky, H. Muckenhuber, H. Grothe, R. Niessner and U. Pöschl, Raman microspectroscopy of soot and related carbonaceous materials: spectral analysis and structural information, *Carbon*, 2005, **43**, 1731–1742.

38 H. Wang, Z. Xu, A. Kohandehghan, Z. Li, K. Cui, X. Tan, T. J. Stephenson, C. K. King'ondu, C. M. Holt, B. C. Olsen, J. K. Tak, D. Harfield, A. O. Anyia and D. Mitlin, Interconnected carbon nanosheets derived from hemp for ultrafast supercapacitors with high energy, *ACS Nano*, 2013, **7**, 5131–5141.

39 J. Chang, Z. Gao, W. Zhao, L. Guo, M. Chu, Y. Tang, D. Wu, F. Xu and K. Jiang, Nitrogen doped microporous carbons with tunable and selective performances in supercapacitor and heterogeneous catalysis, *Electrochim. Acta*, 2016, **190**, 912–922.

40 N. P. Wickramaratne, J. Xu, M. Wang, L. Zhu, L. Dai and M. Jaroniec, Hierarchical mesoporous yolk–shell structured carbonaceous nanospheres for high performance electrochemical capacitive energy storage, *Chem. Mater.*, 2014, **26**, 2820–2828.

41 C. Yuan, X. Liu, M. Jia, Z. Luo and J. Yao, Facile preparation of N-and O-doped hollow carbon spheres derived from poly (o-phenylenediamine) for supercapacitors, *J. Mater. Chem. A*, 2015, **3**, 3409–3415.

42 G. Zhang, S. Sun, D. Yang, J. P. Dodelet and E. Sacher, The surface analytical characterization of carbon fibers functionalized by H$_2$SO$_4$/HNO$_3$ treatment, *Carbon*, 2008, **46**, 196–205.

43 H. A. Andreas and B. E. Conway, Examination of the double-layer capacitance of an high specific-area C-cloth electrode as titrated from acidic to alkaline pHs, *Electrochim. Acta*, 2006, **51**, 6510–6520.

44 X. Fan, Y. Lu, H. Xu, X. Kong and J. Wang, Reversible redox reaction on the oxygen-containing functional groups of an electrochemically modified graphite electrode for the pseudo-capacitance, *J. Mater. Chem.*, 2011, **21**, 18753–18760.

45 V. Khomenko, E. Raymundo-Pinero and F. Beguin, Optimisation of an asymmetric manganese oxide/activated carbon capacitor working at 2 V in aqueous medium, *J. Power Sources*, 2006, **153**, 183–190.

46 M. Kaempgen, C. K. Chan, J. Ma, Y. Cui and G. Gruner, Printable thin film supercapacitors using single-walled carbon nanotubes, *Nano Lett.*, 2009, **9**, 1872–1876.

47 M. Kim, I. Oh and J. Kim, Effects of different electrolytes on the electrochemical and dynamic behavior of electric double layer capacitors based on a porous silicon carbide electrode, *Phys. Chem. Chem. Phys.*, 2015, **17**, 16367–16374.

48 S. X. Wang, C. C. Jin and W. J. Qian, Bi$_2$O$_3$ with activated carbon composite as a supercapacitor electrode, *J. Alloy. Compd.*, 2014, **615**, 12–17.

49 C. C. Hu and C. H. Chu, Electrochemical impedance characterization of polyaniline-coated graphite electrodes for electrochemical capacitors-effects of film coverage/thickness and anions, *J. Electroanal. Chem.*, 2001, **503**, 105–116.

50 P. C. Chen, G. Shen, Y. Shi, H. Chen and C. Zhou, Preparation and Characterization of Flexible Asymmetric Supercapacitors Based on Transition-Metal-Oxide Nanowire/Single-Walled Carbon Nanotube Hybrid Thin-Film Electrodes, *ACS Nano*, 2010, **4**, 4403–4411.

51 W. H. Khoh and J. D. Hong, Solid-state asymmetric supercapacitor based on manganese dioxide/reduced-graphene oxide and polypyrrole/reduced-graphene oxide in a gel electrolyte, *Colloids Surf. A*, 2014, **456**, 26–34.

52 S. Yang, K. Cheng, K. Ye, Y. Li, J. Qu, J. Yin, G. Wang and D. Cao, A novel asymmetric supercapacitor with buds-like Co(OH)$_2$ used as cathode materials and activated carbon as anode materials, *J. Electroanal. Chem.*, 2015, **741**, 93–99.

53 S. Liu, K. S. Hui, K. N. Hui, V. V. Jadhav, Q. X. Xia, J. M. Yun, Y. R. Choa, R. S. Mane and K. H. Kim, Facile synthesis of microsphere copper cobalt carbonate hydroxides electrode for asymmetric supercapacitor, *Electrochim. Acta*, 2016, **188**, 898–908.

54 H. Yi, H. Wang, Y. Jing, T. Peng and X. Wang, Asymmetric supercapacitors based on carbon nanotubes@ NiO ultrathin nanosheets core-shell composites and MOF-derived porous carbon polyhedrons with super-long cycle life, *J. Power Sources*, 2015, **285**, 281–290.

55 R. Qiang, Z. Hu, Y. Yang, Z. Li, N. An, X. Ren, H. Hu and H. Wu, Monodisperse carbon microspheres derived from potato starch for asymmetric supercapacitors, *Electrochim. Acta*, 2015, **167**, 303–310.